TU Delft

Delft University of Technology

Document Version
Final published version

Citation (APA)
Zhang, F., Wu, Z., Gong, Y., Miao, X., Liu, J., Eijt, S., Schut, H., van Dijk, N., Brück, E., & More Authors (2025). Atomic vacancy defect modulated giant magnetocaloric effect in multi-component MnCoNiGeSi based compounds. *Acta Materialia*, *300*, Article 121508. https://doi.org/10.1016/j.actamat.2025.121508

Important note
To cite this publication, please use the final published version (if applicable).
Please check the document version above.

Copyright
In case the licence states “Dutch Copyright Act (Article 25fa)”, this publication was made available Green Open Access via the TU Delft Institutional Repository pursuant to Dutch Copyright Act (Article 25fa, the Taverne amendment). This provision does not affect copyright ownership.
Unless copyright is transferred by contract or statute, it remains with the copyright holder.

Sharing and reuse
Other than for strictly personal use, it is not permitted to download, forward or distribute the text or part of it, without the consent of the author(s) and/or copyright holder(s), unless the work is under an open content license such as Creative Commons.

Takedown policy
Please contact us and provide details if you believe this document breaches copyrights.
We will remove access to the work immediately and investigate your claim.

This work is downloaded from Delft University of Technology.

Green Open Access added to TU Delft Institutional Repository
as part of the Taverne amendment.

More information about this copyright law amendment
can be found at https://www.openaccess.nl.

Otherwise as indicated in the copyright section:
the publisher is the copyright holder of this work and the
author uses the Dutch legislation to make this work public.

Acta Materialia 300 (2025) 121508

Contents lists available at ScienceDirect

Acta Materialia

journal homepage: www.elsevier.com/locate/actamat

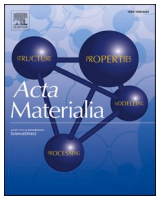

Full length article

Atomic vacancy defect modulated giant magnetocaloric effect in multi-component MnCoNiGeSi based compounds

Fengqi Zhang [a,b,1,*], Ziying Wu [b,c,d,1], Yong Gong [e], Wenjie Li [a], Xuefei Miao [e,*], Jun Liu [e], Yuanguang Xia [f,g], Wen Yin [f,g], Ulrich Lienert [h], Stephan Eijt [b], Zhenduo Wu [i,*], Henk Schut [j], Jakub Čížek [k,*], Niels van Dijk [b], Ekkes Brück [b], Yang Ren [a,l,*]

[a] Department of Physics, JC STEM Lab of Energy and Materials Physics, City University of Hong Kong, Kowloon, Hong Kong SAR, China
[b] Fundamental Aspects of Materials and Energy (FAME), Faculty of Applied Sciences, Delft University of Technology, Mekelweg 15, 2629JB Delft, the Netherlands
[c] Guangdong Provincial Key Laboratory of Optical Information Materials and Technology and Institute of Electronic Paper Displays, South China Academy of Advanced Optoelectronics, South China Normal University, Guangzhou 510006, China
[d] National Center for International Research on Green Optoelectronics, South China Normal University, Guangzhou 510006, China
[e] School of Materials Science and Engineering, Nanjing University of Science and Technology, Nanjing 210094, China
[f] Spallation Neutron Source Science Center, Dalang, Dongguan 523803, China
[g] Institute of High Energy Physics, Chinese Academy of Sciences, Beijing 100049, China
[h] Deutsches Elektronen-Synchrotron DESY, Notkestraße 85, 22607 Hamburg, Germany
[i] City University of Hong Kong (Dongguan), Dongguan, China
[j] Neutron and Positron Methods for Materials, Faculty of Applied Sciences, Delft University of Technology, Mekelweg 15, 2629JB Delft, Netherlands
[k] Faculty of Mathematics and Physics, Charles University, V Holesovickach 2, Prague 8 18000, Czech Republic
[l] Center for Neutron Scattering, City University of Hong Kong, Kowloon, Hong Kong SAR, China

A R T I C L E I N F O

Keywords:
Multi-component magnetocaloric materials
Magnetocaloric effect
Atomic vacancy defects
MnCoNiGeSi alloys
Positron annihilation spectroscopy

A B S T R A C T

Recently, the promising multi-component magnetocaloric materials (Mc-MCMs) are found to have a tunable giant magnetocaloric effect (GMCE) near room-temperature and manifest fruitful functionalities like multi-caloric effects, which are candidates for solid-state caloric applications. Introducing vacancy defects is found to be an efficient method to optimize its GMCE property. However, the responsible mechanism and especially the characteristics of the atomic vacancies are far from being elucidated. Here, we produce direct-solidified MnCoNiGeSi-based Mc-MCMs which exhibit the distinct shift in transition temperature (T_t) upon introducing Mn/Ni vacancies. It is found that T_t decreased significantly in the Mn vacancy materials and increased in the Ni vacancy materials. The first-order transition is maintained and the strength of the magnetic entropy change (Δs_m) was unchanged without degradation. For the Mn vacancy sample the decreased Mn-Mn atomic distance and strengthened covalent bonding can stabilize the high-temperature hexagonal phase, while for the Ni vacancy sample the decreased interatomic distances among different pairs (Mn-Ge, Mn-Mn and Mn-Ni) promote the stabilization of the low-temperature orthorhombic phase. Additionally, the introduced vacancy defects have directly been observed through HAADF-STEM. Positron annihilation results clarified the mono-vacancy nature for these vacancies, and indicate that the Ni positions around the Ni vacancies could partially be occupied by Mn atoms. Our study reveals that introducing atomic vacancy defects can effectively regulate the magnetocaloric properties and provide important fundamental insights into defect engineering of Mc-MCMs.

1. Introduction

Emerging solid-state caloric technologies provide promising strategies for reducing the overall carbon footprint of traditional applications based on the vapor-compression technique [1–3]. Within these techniques, magnetocaloric energy conversion, using magnetocaloric materials (MCMs), has attracted extensive attention for its absence of greenhouse gas emissions and its higher energy utilization efficiency [2,

* Corresponding authors.
E-mail addresses: fzhan7@cityu.edu.hk (F. Zhang), xuefeimiao@njust.edu.cn (X. Miao), zd.wu@cityu-dg.edu.cn (Z. Wu), Jakub.Cizek@mff.cuni.cz (J. Čížek), yangren@cityu.edu.hk (Y. Ren).
[1] These authors contribute equally to this article.

https://doi.org/10.1016/j.actamat.2025.121508
Received 9 April 2025; Received in revised form 26 August 2025; Accepted 3 September 2025
Available online 4 September 2025
1359-6454/© 2025 Acta Materialia Inc. Published by Elsevier Inc. All rights are reserved, including those for text and data mining, AI training, and similar technologies.

4]. The known giant MCMs with a first-order phase transition (FOPT) can provide a noticeable isothermal entropy change (Δs_m) and a sizeable adiabatic temperature change (ΔT_{ad}) [2,5]. Different giant MCMs have been studied, e.g., $Gd_5(Si_2Ge_2)$ [6], $(Mn,Fe)_2(P,X)$ based compounds (X = As, Ge, Si) [7], $La(Fe,Si)_{13}$ based materials [8,9], NiMn-X based magnetic Heusler alloys (X = Al, Ga, In, Sn, Sb, (Co)Ti) [10,11], MnM-X (M = Co/Ni, X = Si/Ge) ferromagnets [12], FeRh [13], and multi-component materials [2,14–17]. Multicomponent alloys (MCAs) or high-entropy alloys are originally sought for within single-phase solid solution to investigate the unexplored central region in phase diagrams [18,19]. These alloys contain five or more elements with a concentration between 35 and 5 at % for each element (composition-based definition), and the total configurational entropy S should be high enough (entropy-based definition), e.g., $S \geq 1.5R$ (a compromise definition) or $S > 1.61R$ where R is the gas constant [20]. Note that the MCAs must be a single-phase solid solution. Therefore, the above definition is also well suitable for the multi-component magnetocaloric materials (Mc-MCMs). Compared to traditional MCMs, the multi-component magnetocaloric materials (Mc-MCMs) offer several advantages [15], e.g., (i) cost reduction and rare-earth element mitigation, which is beneficial for reducing the over-reliance of certain critical elements, e.g., the rare-earth La can be replaced 30–50 % with cheaper Ce for La-Fe-Si alloys [21]. The Mc-MCMs are expected to provide a more sustainable and resource-efficient alternative, e.g., for Fe_2P type compounds. (ii) unique magnetic properties due to their complex microstructures and high configurational entropy [22]. (iii) Mc-MCMs allow for the incorporation of multiple elements. The tailorable composition enables to further fine-tune the properties, including its magnetocaloric response, e.g., reduction of thermal hysteresis (ΔT_{hys}) [23]. (iv) Mc-MCMs with second-order magnetic transition (SOMT) always exhibit a magnetocaloric effect (MCE) over a wide temperature range [24,25]. The versatility makes them promising new candidates for the development of solid-state magnetocaloric cooling/heating technologies.

On the other hand, MnM-X ferromagnets can easily be developed into Mc-MCMs [26–28]. Benefiting from the strong magneto-structural coupling, they undergo a tunable thermoelastic martensitic transformation from high-temperature Ni_2In-type hexagonal (paramagnetic (PM)) to low-temperature TiNiSi-type orthorhombic (ferromagnetic (FM)) phase [29]. Different optimization strategies, including external dopant additions, composition modification and vacancy creation, have been applied to tune its MCE properties. For example, vacancy engineering has been proven to be an effective and efficient strategy to optimize its physical multifunctionality [30–39]. It has been reported that the martensitic transformations can be tuned by vacancy or anti-site disorder in Mn-poor $Mn_{1-x}CoGe$ alloys ($0 \leq x \leq 0.05$) [32]. It was found that the non-magnetic atom vacancy (Ge vacancy) leads to the decrease of the martensitic transition temperature and realized a temperature window where magnetic and martensitic phase transitions can be modified together in $MnCoGe_{1-x}$ alloys [35]. And the magnetostructural transitions and MCE can be optimized by release of trapped thermal vacancies [36]. However, thus far, the detailed mechanism responsible for this approach has not been investigated systematically. For the emerging Mc-MCMs the influence of atomic vacancy defects on the MCE, and the important characteristics of the introduced vacancies have rarely been reported and therefore highly deserve further exploration.

In the present study, different atomic vacancies-engineered quinary MnCoNiGeSi-based Mc-MCMs have been produced and the thermodynamic, magnetic and microstructural properties have been investigated. The responsible mechanism towards well-tuned magnetic properties has been studied from experimental and theoretical aspects. It is worth mentioning that these atomic vacancies have been observed directly, and their characteristics are reported. Our current studies elucidate that introducing atomic vacancy defects can efficiently regulate the magnetocaloric properties in the emerging Mc-MCMs, and provide important complementary insights on further optimization of this materials family.

2. Experimental procedure

High-purity (> 99.9 %) Mn, Co, Ni, Ge, Si raw materials are used to prepare polycrystalline samples using arc-melting and suction-casting under Ar atmosphere. The designed samples have nominal compositions of $Mn_{0.815}Co_{0.37}Ni_{0.815}Ge_{0.75}Si_{0.25}$ ("parent" sample), $Mn_{0.805}Co_{0.37}Ni_{0.815}Ge_{0.75}Si_{0.25}$ ("$Mn_{0.805}$" sample), $Mn_{0.785}Co_{0.37}Ni_{0.815}Ge_{0.75}Si_{0.25}$ ("$Mn_{0.785}$"; sample), $Mn_{0.815}Co_{0.37}Ni_{0.805}Ge_{0.75}Si_{0.25}$ ("$Ni_{0.805}$" sample) and $Mn_{0.815}Co_{0.37}Ni_{0.785}Ge_{0.75}Si_{0.25}$ ("$Ni_{0.785}$" sample), respectively. In order to maintain homogeneity, the ingots were flipped and melted totally 4 times before being suction cast into a copper mold with a diameter of 4 mm. To study the bulk properties of samples without brittleness, the obtained suction-cast rods were remelted at 1873 K for 20 mins in a directional-solidification furnace followed with directionally solidification at a growth rate of 150 μms^{-1} [40]. The actual compositions for different samples have been determined by scanning electron microscopy (SEM) with energy dispersive X-ray spectroscopy (EDS), as shown in Table S1 (Supplementary Information). The morphology of these samples is indicated in Fig. S1 (Supplementary Information), without cracks, holes or other phases.

Differential scanning calorimetry (DSC) measurements were conducted using a commercial TA-Waters Discovery DSC 25 calorimeter. The temperature-dependent magnetization (M-T) and the field-dependent magnetization (M-H) curves were collected in a superconducting quantum interference device (SQUID, Quantum Design MPMS 5XL) magnetometer. And the isothermal M-H measurements at different temperatures were performed by the so-called loop method [41]. Moreover, *in-situ* temperature dependent powder X-ray diffraction (XRD) patterns from 153 to 293 K were collected using an Anton Paar TTK450 temperature chamber and a PANalytical X-pert Pro diffractometer with Cu K_α radiation. The room-temperature (RT) synchrotron high-energy XRD (HE-XRD) measurements (E = 82 KeV) were performed at beamline P21.2 (DESY, Germany). Furthermore, temperature-dependent neutron diffraction (ND) experiments were carried out on the time-of-flight (TOF) powder diffractometer at the BL16 Multi-Physics Instrument (MPI) at the China Spallation Neutron Source (CSNS). About 6 g of powder sample was placed into a vanadium can (8 mm diameter) and diffraction patterns were collected from low temperature (80 K) FM state to high temperature (370 K) PM state. The above obtained XRD and ND patterns were analyzed using Fullprof's implementation of the Rietveld refinement method [42]. In addition, two high-resolution positron annihilation spectroscopy (PAS) techniques called positron lifetime (PL) spectroscopy (identification of types of atomic vacancy defects in the samples) and coincidence Doppler broadening (CDB) (information about the local chemical environment of defects) were applied, equipped with a ^{22}Na radioisotope positron source with an activity of 1 MBq deposited on a 7-μm-thick Kapton foil [43]. The positron source was sealed between two pieces of bulk samples [44]. PL measurements were performed in a digital positron lifetime spectrometer [45], which has a time resolution of (145 ± 1) ps (full width at half maximum (FWHM) of resolution function for ^{22}Na). $>10^7$ positron annihilation events were collected in each PL spectra. The PL spectra were decomposed using a PLRF code, version 19 [46]. Moreover, CDB results were collected at a digital spectrometer with two high-purity Ge detectors [47]. After applying the coincidence and energy restrictions, the CDB system has an energy resolution of 0.99 ± 0.02 keV at 511 keV. $>10^8$ annihilation events were collected in each two-dimensional γ-ray energy spectrum. CDB results are presented as ratio curves with respect to a pure silicon reference. Additionally, transmission electron microscopy (TEM) specimens of $Mn_{0.785}$ and $Ni_{0.785}$ samples were prepared with a focused ion beam system (FIB) using the lift-out method. The high-resolution transmission electron microscopy (HR-TEM) analysis for the $Mn_{0.785}$ and $Ni_{0.785}$ samples was performed using a JEOL JEM-F200 equipment. High angle annular dark field scanning transmission electron microscopy (HAADF-STEM) images were recorded using aberration-corrected transmission electron

microscope (JEOL JEM-ARM300F2) with a monochromator operating at 300 kV. The digital image processing was performed by the Digital-Micrograph software (GMS 3, Gatan Inc).

Electronic Localization Function (ELF) calculations were performed based on density functional theory (DFT) using the Vienna Ab Initio Simulation Package (VASP) [48]. The Perdew-Burke-Ernzerhof (PBE) pseudopotentials were employed with the generalized gradient approximation (GGA) for the exchange-correlation functional. A plane-wave cutoff energy of 500 eV and a 13 × 13 × 13 *k*-point mesh were used. A supercell consisting of 4 unit cells with a hexagonal lattice structure was considered in the simulations. Geometry optimizations for the lattice parameters and atomic site occupancies were carried out based on the experimental lattice parameters.

3. Results and discussion

As shown in Fig. 1a, the *M-T* curves are measured in an applied magnetic field of 1 T for parent, $Mn_{0.805}$, $Mn_{0.785}$, $Ni_{0.805}$ and $Ni_{0.785}$ samples. A strong FOPT from the high-temperature PM state to the low-temperature strong FM state is observed, with transition temperature windows located between 150 and 300 K. Interestingly, compared with the parent sample, the T_t of the samples with Mn vacancies ($Mn_{0.805}$ and $Mn_{0.785}$) were continuously lowered, i.e., $T_t^{heating}$ moved from 248.8 to 242.7 and 210.6 K, respectively. However, the T_t of samples with Ni vacancies ($Ni_{0.805}$ and $Ni_{0.785}$) increased, but the Ni vacancy samples only have T_t shifts of +2.9 K/ % Ni, in comparison to T_t shift of −12.7 K/ % Mn for the Mn vacancy samples with a vacancy concentration of 3 %. Note that after that $Ni_{0.805}$ Ni vacancies have limited impact on T_t change, as observed in $Ni_{0.775}$ sample in Fig. S2 (Supplementary Information). Similarly, the different endothermic and exothermic peaks shifts upon introducing Mn/Ni vacancies can also be observed from zero-field DSC measurements, as presented in Fig. S3 (Supplementary Information). Note that the concomitant specific heat peak for $Ni_{0.785}$ sample could arise from sluggish heat transfer and avalanche type of phase transitions in the main phase, which has been observed before [49]. As shown in Fig. S4a (Supplementary Information), a magnetization separation between cooling and heating curves is found, which could result from the magnetic anisotropy [50,51] because of the direct-solidification production method. Also, compared with the high-temperature hexagonal state, because of the reduced symmetry of the low-temperature orthorhombic state, the number of easy axes can change, therefore a change in the magnetic anisotropy for these samples [51]. This feature will further smear out under a stronger magnetic field (e.g., 1 T), suggesting that the magneto-crystalline anisotropy inside the samples is overcome by the magnetic field. In addition, in the temperature range between 5 and 30 K, a branching and a peak of zero-field cooling (ZFC) curves are also observed for several samples. This behavior could be from the spin-glass or cluster spin-glass state reported in previous MnNiGe-based compounds [52] and similar cases [53–55], where the FM and spin-glass orderings can coexist together at very low temperature. Therefore, the history of the measurement (ZFC and field cooling (FC)) has impact on the *M-T* curves in low magnetic fields. Furthermore, as shown in Fig. S4a (Supplementary Information), the temperature dependent step-like behavior in magnetization for the cooling process at 0.01 T results from a movement of the powder particles in the sample during the magnetic measurement. After fixing the powder particles the steps in low field were found to disappear in Fig. S4b (Supplementary Information). Meanwhile, it is observed that the thermal hysteresis ΔT_{hys} between $T_t^{cooling}$ and $T_t^{heating}$ for Mn and Ni vacancy samples all increased, but Mn vacancy samples have a more

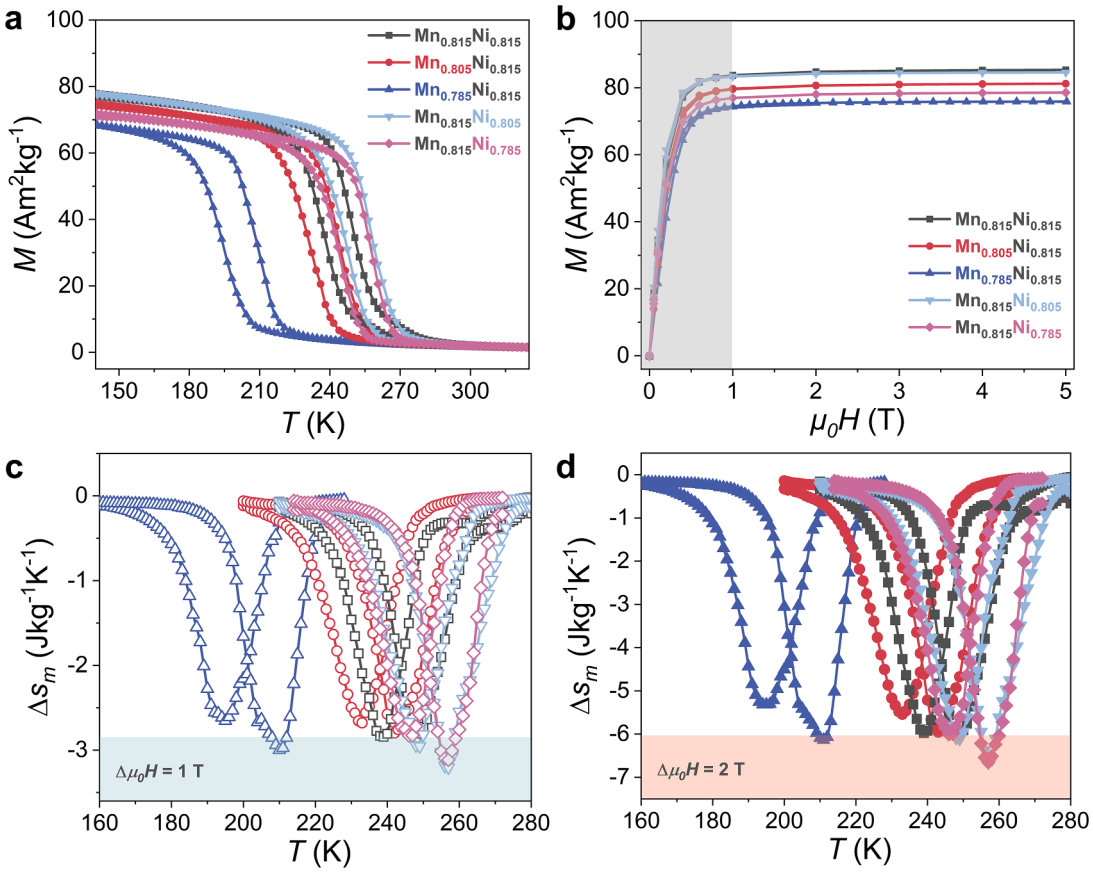

Fig. 1. (a) Iso-field *M-T* curves for different MnNiCoGeSi samples in a field of 1 T (b) Corresponding isothermal *M-H* curves at 5 K. The Δs_m of samples as a function of temperature for both heating and cooling determined for $\Delta\mu_0 H$ of (c) 1 T and (d) 2 T.

significant increment, i.e., from 11.2 (parent) to 16.6 ($Mn_{0.785}$) K. It further indicates that for MnCoNiGeSi-based Mc-MCMs the key parameters of T_t and ΔT_{hys} are more sensitive to the formed Mn vacancy defects. It is worth mentioning that there is an empirical correlation between T_t and chemical composition, when the valence electron concentration parameter (e/a ratio) is considered, which is defined as $e/a = \sum_i (f_i N_i)$, where N_i is the electronic valence number of element and f_i is the atomic weight [56]. The e/a ratio is regarded as an important parameter for the stability of orthorhombic and hexagonal structures [52]. Note that with decreasing e/a ratio a similar opposite trend for the T_t shift has been observed in off-stoichiometric $Mn_{1+x}Ni_{1-x}Ge$ and $Mn_{1-x}Ni_{1+x}Ge$ compounds [56], which exhibit a high sensitivity upon changes in the e/a ratio. Nevertheless, different from the magnetic Heusler-like magnetostructural $Mn_{1.9-x}Ni_xGe$ ($x = 0.850$, 0.855) system, with increasing Mn vacancies lead to an increase in T_t, but no shift in Curie temperature (T_C), where the T_t and T_C are not in the same temperature range [31]. This is consistent with the observation for the $Mn_{1-x}CoGe$ system, where the Mn content was solely changed [32]. The above findings suggest that atomic vacancy defects can not only influence the properties of martensitic structural transition, but also the stability of different phases. Therefore, the e/a reduction is not directly defining the reduction in T_t, but more factors like site occupancy and formed vacancies should be considered. Moreover, as shown in Fig. 1b, Mn vacancy samples show a more significant reduction in saturation magnetization (M_s) compared with Ni vacancy samples. Fig. 1(c and d) presents the calculated Δs_m for cooling and heating processes in the practical field changes $\Delta\mu_0 H$ of 0–1 T and 0–2 T, respectively. The Δs_m values for different field changes $\Delta\mu_0 H$ can be evaluated using the Maxwell relation by [57]:

$$\Delta s_m(T,\ H) = \int_0^H \left(\frac{\partial M}{\partial T}\right)_H d\mu_0 H \tag{1}$$

It is found that after introducing Mn/Ni vacancies the materials maintain their high value of Δs_m without degradation, which further suggests that fine tuning of atomic vacancies can not only achieve a tunable T_t, but provide also good GMCE properties. From the magnetic results, the characteristic temperatures, ΔT_{hys}, M_s and Δs_m for all samples are extracted and summarized in Table 1.

To investigate the structural property changes of these materials, *in-situ* temperature dependent XRD measurements have been utilized between 150 and 300 K. As presented in Fig. 2(a–e), it is clearly visible that a structural transition appears between the high-temperature hexagonal Ni_2In-type structure (space group *P6₃/mmc*) to the low-temperature orthorhombic TiNiSi-type structure (space group *Pnma*). The temperature intervals of phase coexistence have been marked in the figure. From a refinement of the XRD data (e.g. in Fig. S5 (Supplementary Information)), the phase fractions of hexagonal and orthorhombic phases, the lattice parameters and the unit-cell volume (V) was obtained for all samples at different temperatures. These results have been summarized in Tables S2-S4 (Supplementary Information). Fig. 2(f–j) shows the corresponding phase fraction changes for the parent, $Mn_{0.805}$, $Mn_{0.785}$, $Ni_{0.805}$, and $Ni_{0.785}$ samples, respectively. It is observed that the $Mn_{0.785}$ sample shows a remarkable negative shift of the two-phase coexistence region towards lower temperatures. Note that T_t from magnetic measurements is not exactly in the middle of this region, which should be ascribed to the faster heating/cooling rates of XRD scanning due to the first-order transitions that are driven by nucleation and growth [58]. Furthermore, considering the crystallographic relationship between the two structures ($a_{ort} = c_{hex}$, $b_{ort} = a_{hex}$, $c_{ort} = \sqrt{3}a_{hex}$ and $V_{ort} = 2V_{hex}$) [52], the corresponding volume changes from V_{hex} to $V_{ort}/2$ have been calculated, as illustrated in Fig. 2(k–o). Compared with the parent compound, the materials with more Mn/Ni vacancies host a higher volume change during the transition (except $Ni_{0.805}$), and more significant changes attributed to the increased ΔT_{hys} because of the close relationship among them [58–60]. Such a high volume change upon the orthorhombic-hexagonal transition attributes to a remarkable structural entropy change, which can account for over 90 % of the total entropy change for Mn*M*-*X*-based magnetocaloric alloys [61].

Moreover, in comparison to XRD, ND possesses a higher sensitivity to neighboring elements profiting from their different elemental scattering length (Mn:-3.73 fm; Co: 2.49 fm; Ni: 10.3 fm; Ge: 8.18 fm; Si: 4.15 fm). Therefore, it is suitable to employ ND to resolve the site occupation of host atoms and the magnetic moments, and further investigate the subtle microstructural changes on an atomic scale, especially for these MnCoNiGeSi-based Mc-MCMs. Here, we apply *in-situ* temperature-dependent TOF ND measurements for the representative parent, $Mn_{0.805}$ and $Ni_{0.805}$ materials from 80 to 370 K. As illustrated in Fig. 3a, the distinctly different diffraction patterns associated with orthorhombic and hexagonal phases can be observed at high and low temperatures. The main diffraction peaks have been labeled in Q range and there are no impurities are found in the whole Q range. The lattice parameters from ND and XRD results of the structural phases in the PM/FM state for different temperatures have been extracted in Fig. S6 (Supplementary Information) and summarized in Table S5 (Supplementary Information). Meanwhile, the clear crystallographic relationship of a magneto-structural FOPT is demonstrated in Fig. 3b (top). Moreover, the good refinement of ND results in Fig. S7 (Supplementary Information) indicate that for hexagonal phase the preferred site occupancies are: (i) Mn-2*a* (0, 0, 0); (ii) Ni-2*d* (1/3, 2/3, 3/4); (iii) Ge/Si-2*c* (1/3, 2/3, 1/4); (iv) Co atoms are shared with Mn-2*a* and Ni-2*d* sites, while for orthorhombic phase all atoms occupy 4*c* site, but with different position parameters (e.g., for parent compound at 80 K: Mn/Co (0.03271, 0.25000, 0.17880), Ni/Co (0.15259, 0.25000, 0.56048) and Ge/Si (0.75680, 0.25000, 0.62309)) [62]. Note that Mn and Ni vacancies have been observed for the $Mn_{0.805}$, $Mn_{0.785}$, $Ni_{0.805}$ and $Ni_{0.785}$ samples based on Rietveld refinement, at concentrations that are close to the nominal values that are, e.g., 3 % Mn vacancies for the $Mn_{0.785}$ sample and 1 % Ni vacancies for the $Ni_{0.805}$ sample. Taking the orthorhombic phase as an example, Fig. 3b (bottom) illustrates the atomic arrangement of the lattice structure, where Mn-Mn bonds with a honeycomb structure are present. Furthermore, the magnetic refinement including only nuclear structure and magnetic structure have been included in Fig. S7 (Supplementary Information). Utilizing the normal ferromagnetic structure for the magnetic refinement, in Fig. 3c the experimental magnetic moments obtained from ND and magnetization measurements as a function of temperature are shown. Note that for MnNiSi-based compounds the magnetic moment of Ni atoms can be neglected during magnetic refinement [63,64]. Due to the crystal symmetry change the concomitant high-moment to low-moment magnetic transition manifests a large magneto-structural effect [30]. Compared with the $Ni_{0.805}$ sample, it is found that for $Mn_{0.805}$ the reduction in total magnetic moment per formula unit is more noticeable, as a consequence of the decrease in $m_{Mn}(4c)$, while the moment of $m_{Co}(4c)$ is almost unchanged. It is further suggested that the introduced vacancy defects can impact the local chemical environment surrounding the Mn atoms. For example, the resulting coupling distance between the dominant magnetic atoms could be slightly modified, which can strongly influence the magnetic exchange interaction and chemical bonding in the metal-metalloid based intermetallics [57,65–69]. Fig. 3(d–f) presents the temperature dependence of the nearest-neighbor interatomic distances of Mn-Ge, Mn-Mn

Table 1
Summary of the structural temperature upon cooling ($T_t^{cooling}$), the structural temperature upon heating ($T_t^{heating}$), the ΔT_{hys}, M_s at 5 K and 5 T, the Δs_m upon heating with $\Delta\mu_0 H = 1(2)$ T for the mentioned samples.

Sample	$T_t^{cooling}$ (K)	$T_t^{heating}$ (K)	ΔT_{hys} (K)	M_s (Am^2kg^{-1})	$-\Delta s_m$ ($Jkg^{-1}K^{-1}$)
parent	237.6	248.8	11.2	85.3	2.9 (6.0)
$Mn_{0.805}$	231.8	243.4	12.6	81.2	2.8 (6.0)
$Mn_{0.785}$	194.0	210.6	16.6	75.9	3.0 (6.1)
$Ni_{0.805}$	247.2	256.9	9.7	84.5	3.2 (6.7)
$Ni_{0.785}$	244.3	257.6	13.3	78.6	3.1 (6.7)

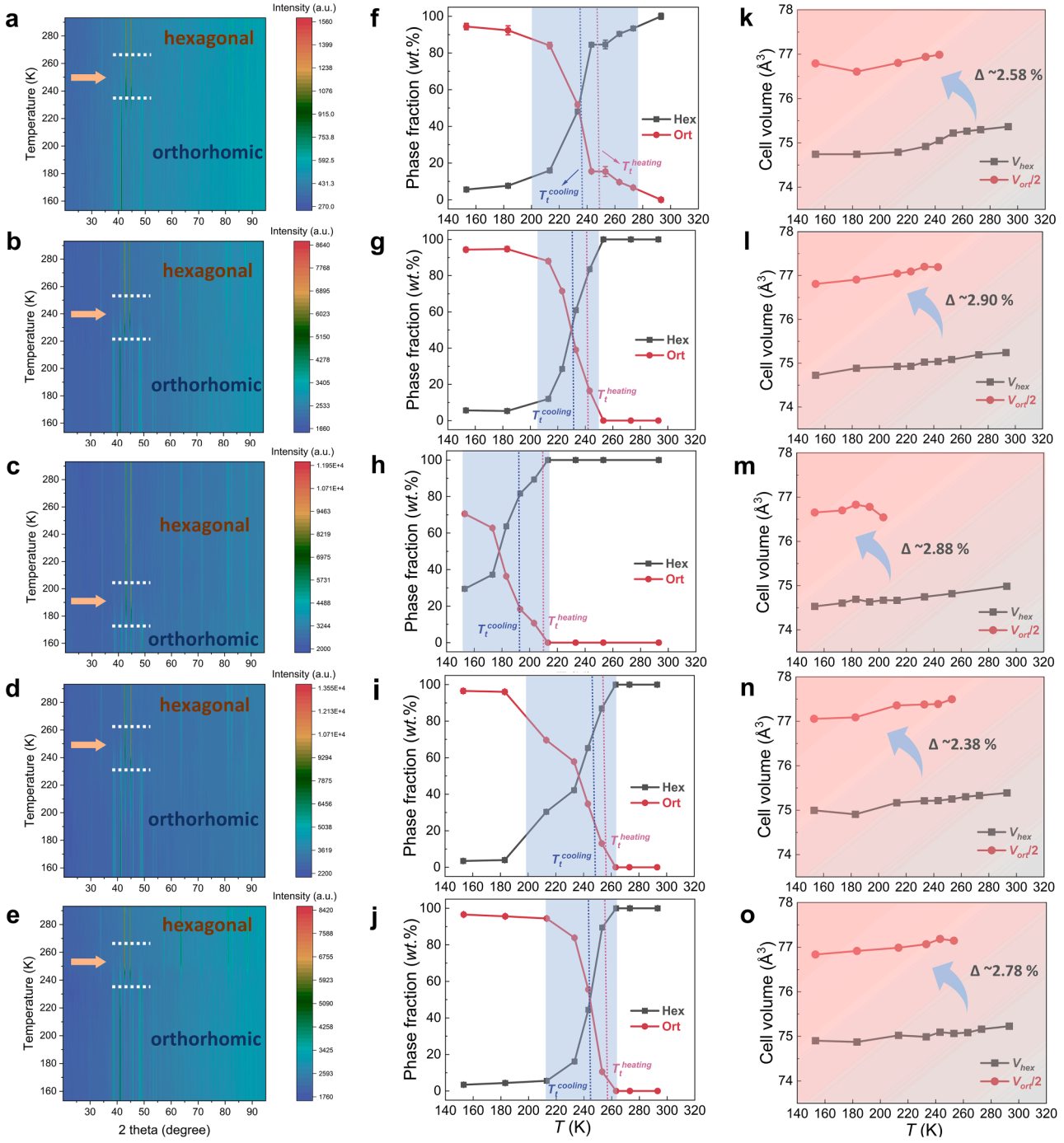

Fig. 2. Contour plots of the temperature-dependent XRD patterns for (a) parent, (b) $Mn_{0.805}$, (c) $Mn_{0.785}$, (d) $Ni_{0.805}$, (e) $Ni_{0.785}$ samples. (f-j) Corresponding phase fraction of hexagonal and orthorhombic phases as a function of temperature for the above samples. (i-l) Temperature dependent unit-cell volume as a function of temperature for the hexagonal and orthorhombic phases for the above samples, presented as the comparison of V_{hex} and $V_{ort}/2$.

and Mn-Ni atomic pairs for the hexagonal and orthorhombic phases in the parent, $Mn_{0.805}$ and $Ni_{0.805}$ samples. For instance, for the hexagonal phase the most remarkable change is that the nearest Mn-Mn distance of the $Mn_{0.805}$ sample is strongly reduced compared with the parent compound, which is accompanied with a slight reduction in Mn-Ge and Mn-Ni distances, while the corresponding distances for the $Ni_{0.805}$ sample are nearly negligible. Previous investigations indicate that changes in interatomic distances are strongly relevant to covalent bonding for the Mn*M*-*X* alloys [62,66,70]. Similar cases for the Fe-substituted MnNiGe [52] and MnCoGeB compounds [66] suggest a strengthening of the covalent bonding between the nearest neighboring atoms can promote the stabilization of the hexagonal structure. Our results show that the shortened interatomic distances especially for Mn-Mn atoms, originating from the introduced Mn vacancies, can further strengthen the covalent bonding among various pairs, which is beneficial for stabilizing the high-temperature hexagonal phase (e.g., decrease T_t) and triggering the magneto-structural FOPT. To get more insight into the influence of different Mn and Ni vacancies on the covalent bonding in the hexagonal structure, ELF calculations are conducted. As demonstrated in Fig. S8 (Supplementary Information), the Mn vacancies result in more localized electrons surrounding Si atoms with a stronger covalent bonding, in comparison to the Ni vacancies

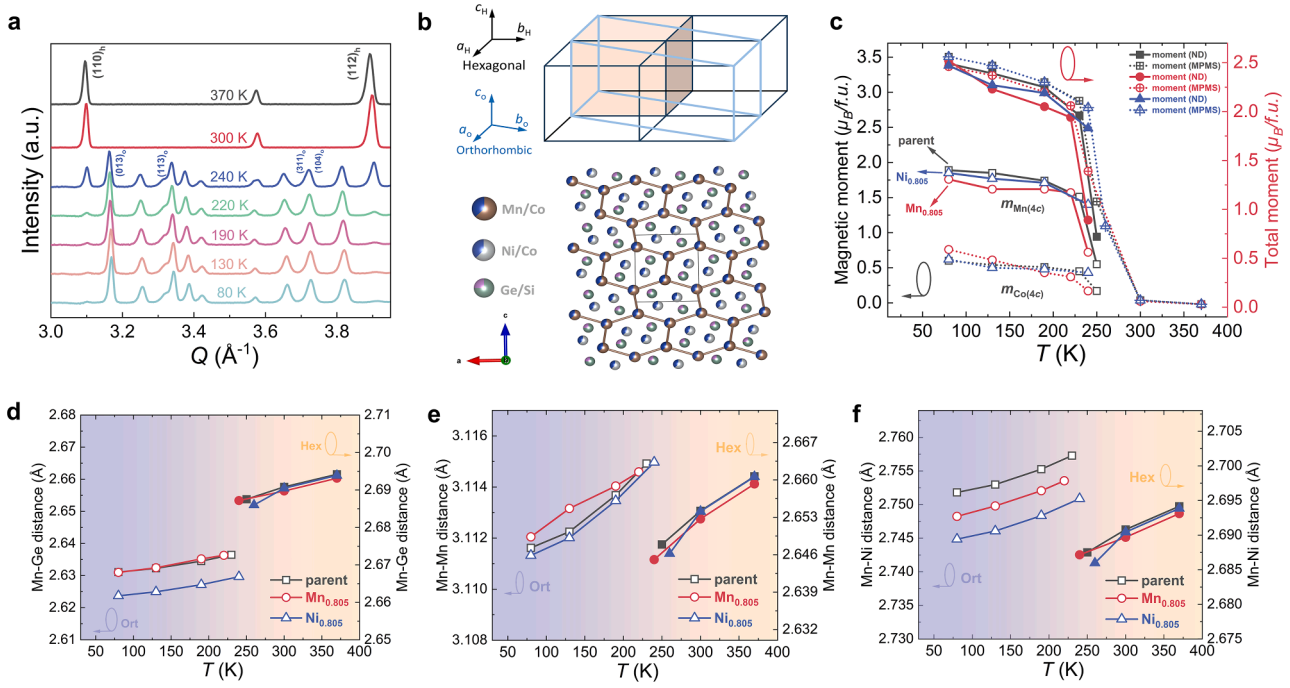

Fig. 3. (a) Temperature-dependent ND of the representative $Mn_{0.785}$ sample from 80 to 370 K, indicating the structural transition from orthorhombic to hexagonal phase. (b) Top-schematic representation of the crystallographic relationship between hexagonal (black) and orthorhombic (blue) phases. Bottom-illustration of Mn-Mn bonds within orthorhombic lattice structure. (c) Experimental magnetic moments obtained from ND and SQUID magnetization measurements as a function of temperature for parent, $Mn_{0.805}$ and $Ni_{0.805}$ samples. The individual moments related to Mn(4*c*) and Co(4*c*) guide to left *y* axis. The total moments guide to right *y* axis. Corresponding interatomic distances of (d) Mn-Ge, (e) Mn-Mn and (f) Mn-Ni for hexagonal (yellow) and orthorhombic (purple) phases as a function of temperature for above compounds, determined from ND, respectively.

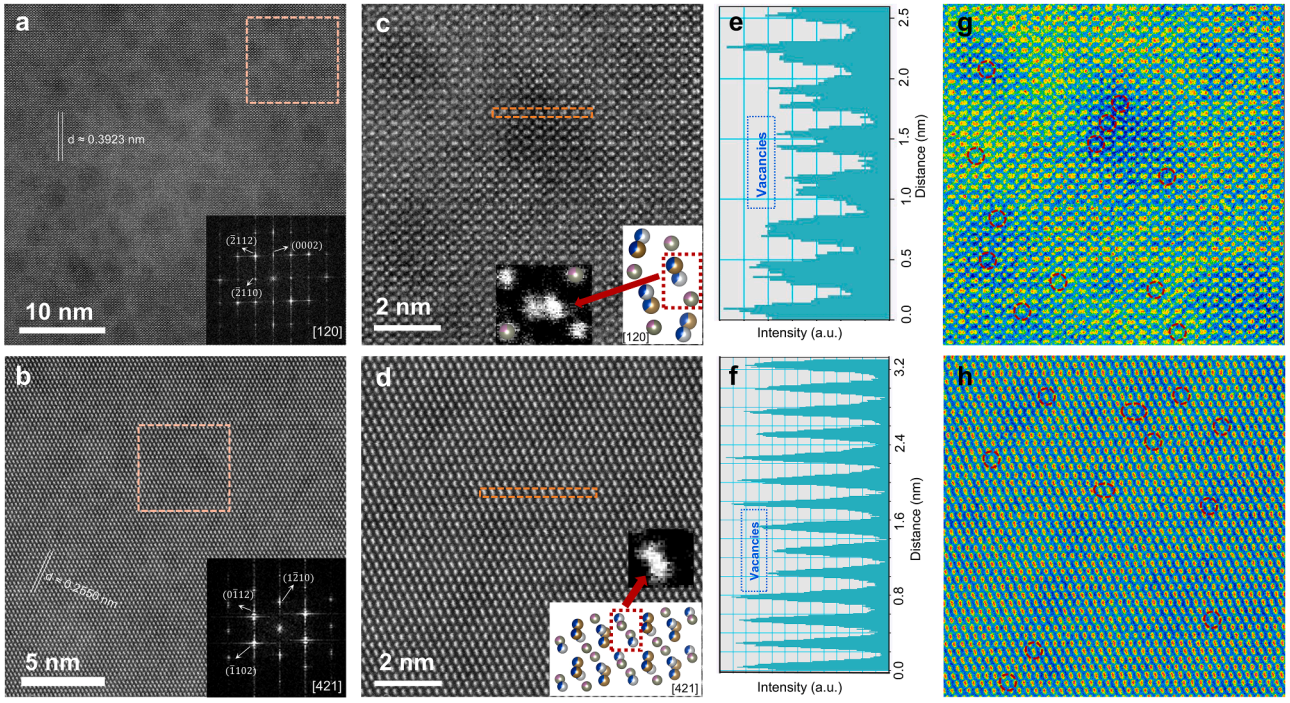

Fig. 4. Microstructural observation related to $Mn_{0.785}$ and $Ni_{0.785}$ materials. (a-b) HAADF-STEM images along [120] and [421] directions for $Mn_{0.785}$ and $Ni_{0.785}$ samples, respectively. The inset is the corresponding FFT patterns in the regions indicated by the yellow box. (c-d) High-resolution HAADF-STEM images for $Mn_{0.785}$ and $Ni_{0.785}$ samples, respectively. The insets show the observation of atoms in real space and modeled crystal structures along different directions. (e-f) Line intensity profiles are extracted from the yellow boxes in (c-d) for $Mn_{0.785}$ and $Ni_{0.785}$ samples, respectively. The positions of atomic vacancy defects can be distinguished according to the intensity of the peaks. (g-h) Pseudo-colored HAADF-STEM images on the basis of (c-d) for $Mn_{0.785}$ and $Ni_{0.785}$ samples, respectively. The potential atomic vacancies have been marked as red circles.

counterpart. Our ELF results provide further insights into the origin of the decreased T_t for Mn vacancy samples and the increased T_t for Ni vacancy samples. In addition, it is found that the magnetic ground state of the orthorhombic phase is critical to the nearest-neighbor Mn-Mn distance [71,72]. In contrast to the atomic changes of the hexagonal phase, for orthorhombic phase the nearest-neighbor Mn-Mn distance of the $Mn_{0.805}$ sample shows a remarkable increment relative to the parent sample with decreasing temperature, compared with the slight decrease for the $Ni_{0.805}$ sample. Consequently, the longer Mn-Mn interatomic distance could cause a weaker covalent bonding, which is quite the opposite to the hexagonal situation. Moreover, Liu and coworkers pointed out that atomic vacancies could destroy the chemical bonding, e.g., for the so important Mn-Mn honeycomb connections (see Fig. 3b (bottom)), which may lead to the destabilization of the orthorhombic phase at lower temperature and the weakening of the elastic modulus of the hexagonal phase [32]. It can make the structural transition occur at lower temperature, and thus a smaller thermodynamic driving force is needed to overcome the energy barrier of nucleation [32,73]. Moreover, additional variations in the Mn-Ge and Mn-Ni distances are also observed in Fig. 3d and 3f. Compared with the parent and the $Mn_{0.805}$ samples, it is clearly visible that for the $Ni_{0.805}$ sample both distances are simultaneously decreased, indicating the strengthened covalent bonding among the Mn-Ge and Mn-Ni pairs. Therefore, together with Mn-Mn changes the stronger bonding resulting from the induced Ni vacancies can further stabilize the low-temperature orthorhombic phase (e.g., increase T_t), in line with above ELF observations. The introduced Mn and Ni atomic vacancy defects play different roles in the characteristics of the transition, which critically depends on subtle changes of different interatomic distances among the metal-metalloid pairs.

Numerous studies investigated the influence of vacancy defects on the regulation of the MCE performance [30–39]. However, experimental reports associated with the direct observation of vacancies, as well as its nature, are rare. As shown in Fig. 4(a and b), the microstructure at RT for the $Mn_{0.785}$ and $Ni_{0.785}$ samples has been obtained using HAADF-STEM. The corresponding fast Fourier transform (FFT) for the selected region demonstrates its hexagonal structure ($P6_3/mmc$) and the main crystal planes have been indexed. In Fig. 4(c-d) the high-resolution HAADF--STEM images show the observation of atoms in real space along different directions, and the atoms (clusters) have been compared with the modeled crystal structures. Note that the atomic arrangement has been determined based on previous preferred occupancies extracted from our ND study. What's more, it is well known that the HAADF-STEM image contrast I is approximately proportional to the square of atomic number Z ($I \propto Z^2$) [74]. Therefore, the lightness of different atomic columns can be utilized to distinguish the different elemental atoms, chemical variations and atomic vacancy defects. For example, the monolayer intensity profiles in Fig. 4(e and f) show the perturbations in contrast difference along the yellow box in Fig. 4(c and d), and the positions of atomic vacancy defects for $Mn_{0.785}$ and $Ni_{0.785}$ samples can be directly captured according to the intensity of the peaks [75,76]. Furthermore, after pseudo-color processing for Fig. 4(c and d), more pronounced atomic vacancies for these two samples can be observed from the clearer contrast difference, as present in Fig. 4(g) and 4(h), respectively. In addition, HR-TEM-EDS experiments have been performed for the typical $Mn_{0.785}$ and $Ni_{0.785}$ samples. As shown in Fig. S9 and S10 (Supplementary Information), it is found that all elements are homogenously distributed and there is no chemical segregation for $Mn_{0.785}$ and $Ni_{0.785}$ samples, respectively. Furthermore, we employ EDS-line scanning for these two samples, as present in Fig. S11 (Supplementary Information). Especially, it is observed there is no remarkable compositional changes within 20 nm distance from the EDS-line scanning crossing the area with contrast difference. Therefore, it is indicated that the samples have good chemical stability and we can exclude nanoscale short-range chemical segregation/clustering. Although the introduced vacancy defects have directly been observed through HAADF-STEM, the detailed properties of the Mn/Ni vacancies and the local chemical environment next to the vacancies need to be further verified.

To further understand the vacancy defects from a microscopic perspective, positron annihilation spectroscopy (PAS) is employed for different complex multi-component alloys [77–79]. PAS is a non-destructive method and can efficiently obtain information of open-volume defects like vacancies with a high sensitivity, because of the strong affinity between positrons and defects resulting in a positron-electron pair annihilation process [2,43,80,81]. Note that the synchrotron HE-XRD experiments have excluded the influence of impurities inside the samples, as presented in Fig. S12 (Supplementary Information). For different PAS methods, the PL experiments can make a distinction between the possible types and establish the concentration of the vacancy defects inside the sample, while CDB enables characterization of the local chemical environment of vacancies. The results of the PL measurements are summarized in Table S6 (Supplementary Information). It shows that all alloys exhibit a single-component PL spectrum characterized by a lifetime τ_2, which is significantly higher than the bulk positron lifetime and is close to the value expected for positrons trapped in mono-vacancies [82,83]. The alloys contain a high concentration of vacancies and all positrons are found to be trapped in these vacancies (saturated positron trapping). In Fig. 5a the lifetime of trapped positrons, τ_2, is plotted as a function of the Mn/Ni ratio. The slight increasing of τ_2 stems from an increase in the local electron density at the site of the vacancies, indicating a gradual change in the local chemical environment with increasing Ni concentration and/or in the size of the positron trapping vacancy.

Moreover, the CDB ratio curves related to a pure silicon reference are plotted in Fig. 5b. For comparison, the ratio curves for reference samples of pure Mn, Co, Ni, and Ge are also included. It is noticed that the ratio curves for all alloys are similar and show a maximum around 13×10^{-3} m_0c, which arises from the contribution of positrons that annihilate with 3d electrons. As virtually all positrons are trapped at vacancies, the ratio curves represent the momentum distribution corresponding to the local chemical environment of these vacancies. Hence, it demonstrates that the chemical environment of vacancies in all alloys is similar. To gain a better understanding of how different alloying elements contribute to the ratio curves of the studied alloys, the ratio curves of reference samples of pure elements (Mn, Co, Ni, Ge, and Si) are also collected. From the comparison, we can observe that the shape of the ratio curves is similar to that of pure Mn and Ge. It suggests that the chemical environment of vacancies in the studied alloys is enriched with Mn and Ge. Additionally, the slight shift of the rising edge in the ratio curves of the alloys, which occurs with an increasing Mn/Ni ratio, can be linked to increasing contribution of Mn due to a higher concentration of Mn around the vacancies. To obtain a more quantitative comparison, the ratio curves of MnCoNiGeSi-based alloys can be approximated in the high momentum region by a superposition of the ratio curves for pure elements [84]:

$$\rho(p) = \xi_{Mn}\rho_{Mn}(p) + \xi_{Co}\rho_{Co}(p) + \xi_{Ni}\rho_{Ni}(p) + \xi_{Ge}\rho_{Ge}(p) + \xi_{Si}\rho_{Si}(p) \quad (2)$$

where $\rho(p)$ represent ratio curves for pure Mn, Co, Ni, Ge, and Si and the coefficients ξ are fractions of positrons trapped in vacancies and annihilated in the vicinity of the element. These coefficients are not fully independent but always fulfill the condition $\xi_{Mn} + \xi_{Co} + \xi_{Ni} + \xi_{Ge} + \xi_{Si} = 1$ [84]. Assuming that the vacancies in the alloys are distributed completely randomly, it means that there is no preference among the constituent elements to be near these vacancies, and the coefficients would equal to the concentrations of the corresponding elements in the alloys. Considering the model of a fully random distribution of vacancies, the calculated superposition ratio curve (dashed line in Fig. 5b, nominal composition for the parent sample) evidently cannot align with the experimental data. The discrepancy indicates that the actual chemical environment around the vacancies is not random, in other words, certain elements tend to segregate preferentially around the vacancies, which is also observed in other multi-component cases [84,

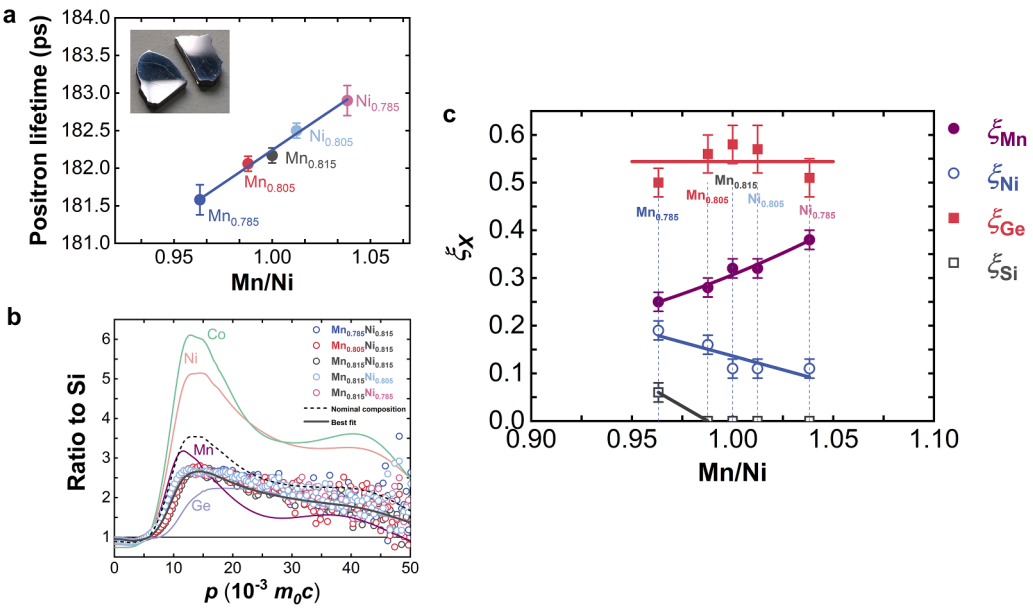

Fig. 5. (a) Lifetime τ_2 of positrons trapped at defects plotted as a function of the Mn to Ni ratio for parent, $Mn_{0.785}$, $Mn_{0.805}$, $Ni_{0.805}$ and $Ni_{0.785}$ alloys. The inset shows the polished bulk samples for the measurements. (b) Ratio curves related to pure Si reference for different samples. For comparison the ratio curves for reference samples of pure elements (Mn, Co, Ni, Ge) are plotted in the figure as well. Since all ratio curves are related to Si the ratio curve for pure Si a straight line at unity. (c) Fractions ξ for x = Mn, Ni, Ge, Si obtained from fitting of CDB ratio curves using Eq. (2). Not that the fractions for Co are zero.

85]. Therefore, the adjusted coefficients have been achieved and the fitting results (i.e., for parent sample) are illustrated (solid line in Fig. 5b), which shows a good representation of the experimental points. The coefficients obtained from the fitting process for all studied alloys are summarized in Table S7 (Supplementary Information). The closest agreement was found under the assumption that vacancies are preferentially surrounded by Mn, Ni, and Ge atoms. And the concentration of Si in the vicinity of vacancies is very low, as a non-zero coefficient was obtained only for the $Mn_{0.785}$ sample. The coefficient for Co, remains zero across all studied alloys, indicating that Co is not located near the vacancies. Fig. 5c illustrates the development of the chemical environment of vacancies with composition changes, displaying the fractions of Mn, Ni, Ge, and Si obtained from fitting as a function of the Mn/Ni ratio. It further indicates that, with an increasing Mn/Ni ratio, vacancies are surrounded by a higher concentration of Mn, while the concentration of Ni around vacancies gradually decreases. In contrast, the concentration of Ge around the vacancies appears to be nearly independent of the Mn/Ni ratio. These findings suggest that the increase in the lifetime τ_2 of positrons trapped at vacancies, with a rising Mn/Ni ratio shown in Fig. 5a, is likely due to the increasing concentration of Mn atoms in the environment of the vacancy at the expense of the Ni atoms. This is in line with a decrease in concentration of Mn vacancies and increase in concentration of Ni vacancies for larger values of the Mn/Ni ratio. Combining the crystal structure analysis and the ND results, it is concluded that the original Ni positions around introduced Ni vacancies could be preferentially and partially occupied by a certain amount of Mn atoms. This is consistent with the limited increase in T_t for the $Ni_{0.785}$ sample. The above results mean that a rational control of the type and concentration of atomic vacancy defects provides a way to control the strong magneto-structurally coupled transition in these emerging Mc-MCMs.

4. Conclusions

In summary, different Mn and Ni atomic vacancies-engineered quinary MnCoNiGeSi-based Mc-MCMs have successfully been synthesized, and their basic thermodynamic, magnetic and microstructural properties have been investigated utilizing DSC, SQUID, XRD, ND, STEM and PAS. Compared with the parent sample, it is found that T_t obviously decreases in Mn vacancy materials and increases in Ni vacancy materials, while the FOPT is maintained and Δs_m shows no degradation. The distinct behavior introduced by different types of Mn and Ni vacancies is understood from experimental and theoretical perspectives, and it could be attributed in terms of metastable microstructural changes. For instance, for the Mn vacancy sample the decreased Mn-Mn atomic distance and strengthened covalent bonding can stabilize the high-temperature hexagonal phase, and vice versa, for the Ni vacancy sample the decreased interatomic distances among different pairs (Mn-Ge, Mn-Mn and Mn-Ni) promote the stabilization of the low-temperature orthorhombic phase. Additionally, the introduced vacancy defects have directly been observed in the studied samples. The PL and CDB results clarify the presence of mono-vacancies. With an increasing Mn/Ni ratio, the concentration of Mn vacancies reduces while the concentration of Ni vacancies increases, in which the vacancies are surrounded by a higher concentration of Mn atoms, and the original Ni sites around introduced Ni vacancies could be preferentially and partially occupied by a certain amount of Mn atoms. Our present study indicates that introducing different atomic vacancy defects can efficiently tailor the MCE properties of the emerging Mc-MCMs by a modification of the microstructure, which enhances their prospects for future applications.

Data availability

Data will be made available on request.

CRediT authorship contribution statement

Fengqi Zhang: Writing – review & editing, Writing – original draft, Project administration, Methodology, Investigation, Formal analysis, Data curation, Conceptualization. **Ziying Wu:** Writing – review & editing, Methodology, Investigation, Data curation, Conceptualization. **Yong Gong:** Investigation, Data curation. **Wenjie Li:** Investigation, Data curation. **Xuefei Miao:** Writing – review & editing, Visualization, Methodology, Investigation, Formal analysis. **Jun Liu:** Investigation, Formal analysis. **Yuanguang Xia:** Investigation, Data curation. **Wen Yin:** Investigation, Data curation. **Ulrich Lienert:** Investigation, Data

curation. **Stephan Eijt:** Writing – review & editing, Methodology, Investigation, Data curation. **Zhenduo Wu:** Writing – review & editing, Resources, Investigation, Formal analysis, Data curation. **Henk Schut:** Writing – review & editing, Methodology, Investigation. **Jakub Čížek:** Writing – review & editing, Writing – original draft, Resources, Methodology, Investigation, Data curation. **Niels van Dijk:** Writing – review & editing, Investigation, Formal analysis, Data curation. **Ekkes Brück:** Writing – review & editing, Visualization, Resources, Project administration, Investigation. **Yang Ren:** Writing – review & editing, Supervision, Resources, Project administration, Funding acquisition, Formal analysis.

Declaration of competing interest

The authors declare that they have no known competing financial interests or personal relationships that could have appeared to influence the work reported in this paper.

Acknowledgments

The authors thank X. Miao acknowledges National Natural Science Foundation of China (Grant No 52571222) for financial support. Anton Lefering, Bert Zwart, Yan Li (CSNS) and Prof. Jianrong Gao (Northeastern University) for their technical assistance. This work was supported by the open research fund of CSNS (Grant No KFKT2022B04, KFKT2022A05). F.Q. Zhang and Y. Ren acknowledge financial support from City University of Hong Kong (Project No 9610533). Z.D. Wu acknowledges the support by the National Natural Science Foundation of China (No 52201190), and by Guangdong Basic and Applied Basic Research Foundation (No 2024A1515010964). F.Q. Zhang and Y. Ren would like to express sincere appreciation to the Hong Kong SAR government for supporting the research under the Global STEM Professorship, and to the Hong Kong Jockey Club for supporting the research under the JC STEM Lab of Energy and Materials Physics. We acknowledge DESY (Hamburg, Germany), a member of the Helmholtz Association HGF, for the provision of experimental facilities. Parts of this research were carried out at PETRA III and we would like to thank (Dr. Sangho Jeon) for assistance in using beamlines P21.2. Beamtime was allocated for proposal (I-20240028).

Supplementary materials

Supplementary material associated with this article can be found, in the online version, at doi:10.1016/j.actamat.2025.121508.

References

[1] X. Moya, N.D. Mathur, Caloric materials for cooling and heating, Science (1979) 370 (2020) 797.
[2] F.Q. Zhang, X.F. Miao, N. van Dijk, E. Brück, Y. Ren, Advanced magnetocaloric materials for energy conversion: recent progress, opportunities, and perspective, Adv. Energy Mater. 14 (2024) 2400369.
[3] K. Klinar, J.Y. Law, V. Franco, X. Moya, A. Kitanovski, Perspectives and energy applications of magnetocaloric, pyromagnetic, electrocaloric, and pyroelectric materials, Adv. Energy Mater. 14 (2024) 2401739.
[4] A. Kitanovski, Energy applications of magnetocaloric materials, Adv. Energy Mater. 10 (2020) 1903741.
[5] E. Brück, Developments in magnetocaloric refrigeration, J. Phys. D. Appl. Phys. 38 (2005) R381.
[6] V.K. Pecharsky, K.A. Gschneidner, Giant magnetocaloric effect in Gd5(Si2Ge2), Phys. Rev. Lett. 78 (1997) 4494.
[7] O. Tegus, E. Brück, K.H.J. Buschow, F.R. de Boer, Transition-metal-based magnetic refrigerants for room-temperature applications, Nature 415 (2002) 150.
[8] F.X. Hu, B.G. Shen, J.R. Sun, Z.H. Cheng, G.H. Rao, X.X. Zhang, Influence of negative lattice expansion and metamagnetic transition on magnetic entropy change in the compound LaFe11.4Si1.6, Appl. Phys. Lett. 78 (2001) 3675.
[9] A. Fujita, S. Fujieda, K. Fukamichi, Y. Yamazaki, Y. Iijima, Giant magnetic entropy change in hydrogenated La(Fe0.88Si0.12)13Hy compounds, Mater. Trans. 43 (2002) 1202.
[10] A. Planes, L. Manosa, M. Acet, Magnetocaloric effect and its relation to shape-memory properties in ferromagnetic Heusler alloys, J. Phys.-Condens Mat. 21 (2009) 233201.
[11] Z.Y. Wei, E.K. Liu, J.H. Chen, Y. Li, G.D. Liu, H.Z. Luo, X.K. Xi, H.W. Zhang, W. H. Wang, G.H. Wu, Realization of multifunctional shape-memory ferromagnets in all-d-metal heusler phases, Appl. Phys. Lett. 107 (2015) 022406.
[12] N.T. Trung, L. Zhang, L. Caron, K.H.J. Buschow, E. Brück, Giant magnetocaloric effects by tailoring the phase transitions, Appl. Phys. Lett. 96 (2010) 172504.
[13] M.P. Annaorazov, K.A. Asatryan, G. Myalikgulyev, S.A. Nikitin, A.M. Tishin, A. L. Tyurin, Alloys of the Fe-Rh system as a new class of working material for magnetic refrigerators, Cryogenics. (Guildf) 32 (1992) 867.
[14] L.L. Han, S.Y. Zhu, Z.Y. Rao, C. Scheu, D. Ponge, A. Ludwig, H.B. Zhang, O. Gutfleisch, H. Hahn, Z.M. Li, D. Raabe, Multifunctional high-entropy materials, Nat. Rev. Mater. 9 (2024) 846.
[15] J.Y. Law, V. Franco, Pushing the limits of magnetocaloric high-entropy alloys, APL. Mater. 9 (2021) 080702.
[16] J.Y. Law, V. Franco, Review on magnetocaloric high-entropy alloys: design and analysis methods, J. Mater. Res. 38 (2023) 37.
[17] W.T. Zhang, X.Q. Wang, F.Q. Zhang, X.Y. Cui, B.B. Fan, J.M. Guo, Z.M. Guo, R. Huang, W. Huang, X.B. Li, M.R. Li, Y. Ma, Z.H. Shen, Y.G. Sun, D.Z. Wang, F. Y. Wang, L.Q. Wang, N. Wang, T.L. Wang, W. Wang, X.Y. Wang, Y.H. Wang, F. J. Yu, Y.Z. Yin, L.K. Zhang, Y. Zhang, J.Y. Zhang, Q. Zhao, Y.P. Zhao, X.D. Zhu, Y. Sohail, Y.N. Chen, T. Feng, Q.L. Gao, H.Y. He, Y.J. Huang, Z.B. Jiao, H. Ji, Y. Jiang, Q. Li, X.M. Li, W.B. Liao, H.J. Lin, H. Liu, Q. Liu, Q.F. Liu, W.D. Liu, X. J. Liu, Y. Lu, Y.P. Lu, W. Ma, X.F. Miao, J. Pan, Q. Wang, H.H. Wu, Y. Wu, T. Yang, W.M. Yang, Q. Yu, J.Y. Zhang, Z.G. Chen, L. Mao, Y. Ren, B.L. Shen, X.L. Wang, Z. Jia, H. Zhu, Z.D. Wu, S. Lan, Frontiers in high entropy alloys and high entropy functional materials, Rare Metals. 43 (2024) 4639.
[18] B. Cantor, I.T.H. Chang, P. Knight, A.J.B. Vincent, Microstructural development in equiatomic multicomponent alloys, Mat. Sci. Eng. a-Struct. 375 (2004) 213.
[19] J.W. Yeh, S.K. Chen, S.J. Lin, J.Y. Gan, T.S. Chin, T.T. Shun, C.H. Tsau, S.Y. Chang, Nanostructured high-entropy alloys with multiple principal elements: novel alloy design concepts and outcomes, Adv. Eng. Mater. 6 (2004) 299.
[20] D.B. Miracle, O.N. Senkov, A critical review of high entropy alloys and related concepts, Acta. Mater. 122 (2017) 448.
[21] J.W. Lai, H. Sepehri-Amin, X. Tang, J. Li, Y. Matsushita, T. Ohkubo, A.T. Saito, K. Hono, Reduction of hysteresis in (La1-xCex)y(MnzFe11.4-z)Si11.6 magnetocaloric compounds for cryogenic magnetic refrigeration, Acta Mater. 220 (2021) 117286.
[22] Y. Yuan, Y. Wu, X. Tong, H. Zhang, H. Wang, X.J. Liu, L. Ma, H.L. Suo, Z.P. Lu, Rare-earth high-entropy alloys with giant magnetocaloric effect, Acta Mater. 125 (2017) 481.
[23] A. Díaz-García, J.Y. Law, L.M. Moreno-Ramírez, V. Franco, Stress-relieved Fe-Mn-Ni-Ge-Si high-entropy alloys: a path for enhancing the magnetocaloric response, Scripta Mater 258 (2025) 116492.
[24] W.H. Zhu, L. Ma, M.F. He, Z.K. Li, H.Z. Zhang, Q.R. Yao, G.H. Rao, K.P. Su, X. C. Zhong, Z.W. Liu, X.Q. Gao, Large refrigerant capacity induced by table-like magnetocaloric effect in high-entropy alloys TbDyHoEr, Adv. Eng. Mater. 25 (2023) 2201770.
[25] X.J. Wang, S.T. Zong, Y. Zhang, Z.J. Mo, J.W. Qiao, P.K. Liaw, The large magnetocaloric effect in GdErHoCoM (M = Cr and Mn) high-entropy alloy ingots with orthorhombic structures, Appl. Phys. Lett. 124 (2024) 122412.
[26] J.Y. Law, A. Díaz-García, L.M. Moreno-Ramírez, V. Franco, Increased magnetocaloric response of FeMnNiGeSi high-entropy alloys, Acta Mater. 212 (2021) 116931.
[27] Y. Guo, T.T. Zhang, Z.S. Zhang, B. Chen, W.H. Guo, S. Pan, Y. Gong, Y.Q. Bai, Y. Y. Gong, J. Liu, X.F. Miao, F. Xu, Large reversible magnetocaloric effect in high-entropy MnFeCoNiGeSi system with low-hysteresis magnetostructural transformation, APL. Mater. 10 (2022) 091107.
[28] X.Y. Wang, H.C. Xuan, M.J. Ji, F.H. Chen, Z.D. Han, P.D. Han, J.W. Qiao, Large barocaloric and magnetocaloric effects in MnFe0.8+xNi1.2-xSiGe0.5 high-entropy intermetallics, Appl. Phys. Lett. 124 (2024) 092411.
[29] J. Liu, Y.Y. Gong, Y.R. You, X.M. You, B.W. Huang, X.F. Miao, G.Z. Xu, F. Xu, E. Brück, Giant reversible magnetocaloric effect in MnNiGe-based materials: minimizing thermal hysteresis via crystallographic compatibility modulation, Acta Mater. 174 (2019) 450.
[30] J.T. Wang, D.S. Wang, C.F. Chen, O. Nashima, T. Kanomata, H. Mizuseki, Y. Kawazoe, Vacancy induced structural and magnetic transition in MnCo1-xGe, Appl. Phys. Lett. 89 (2006) 262504.
[31] C.L. Zhang, D.H. Wang, Q.Q. Cao, Z.D. Han, H.C. Xuan, Y.W. Du, Magnetostructural phase transition and magnetocaloric effect in off-stoichiometric Mn1.9-xNixGe alloys, Appl. Phys. Lett. 93 (2008) 122505.
[32] E.K. Liu, W. Zhu, L. Feng, J.L. Chen, W.H. Wang, G.H. Wu, H.Y. Liu, F.B. Meng, H. Z. Luo, Y.X. Li, Vacancy-tuned paramagnetic/ferromagnetic martensitic transformation in Mn-poor Mn1-xCoGe alloys, Europhys. Lett. 91 (2010) 17003.
[33] J. Liu, K. Skokov, O. Gutfleisch, Magnetostructural transition and adiabatic temperature change in Mn-Co-Ge magnetic refrigerants, Scripta Mater 66 (2012) 642.
[34] J.C. Lin, P. Tong, K. Zhang, H.Y. Tong, X.G. Guo, C. Yang, Y. Wu, M. Wang, S. Lin, L. Chen, W.H. Song, Y.P. Sun, Colossal negative thermal expansion with an extended temperature interval covering room temperature in fine-powdered Mn0.98CoGe, Appl. Phys. Lett. 109 (2016) 241903.
[35] L.F. Bao, W.D. Huang, Y.J. Ren, Tuning martensitic phase transition by non-magnetic atom vacancy in MnCoGe alloys and related giant magnetocaloric effect, Chinese Phys. Lett. 33 (2016) 077502.
[36] Y. Li, Q.Q. Zeng, Z.Y. Wei, E.K. Liu, X.L. Han, Z.W. Du, L.W. Li, X.K. Xi, W.H. Wang, S.G. Wang, G.H. Wu, An efficient scheme to tailor the magnetostructural transitions by staged quenching and cyclical ageing in hexagonal martensitic alloys, Acta. Mater. 174 (2019) 289.

[37] Y. Song, S.C. Ma, F. Yang, Z.S. Zhang, Y.X. Zhang, H. Zeng, S.U. Rehman, G.F. Feng, X.H. Luo, C.C. Chen, Z.S. Lu, Z.C. Zhong, Co-vacancy induced magneto-structural transformation in Co and Ge bidirectional-regulation MnCoGe systems, J. Alloy. Compd. 819 (2020) 153061.
[38] R.C. Li, L.L. Wang, P.L. Miao, C.H. Xie, X.F. Tang, G.J. Tan, Fine tuning of Mn/Co vacancies for optimized magnetocaloric performance in MnCoGe alloys, J. Magn. Magn. Mater. 603 (2024) 172224.
[39] R. Roy, S.K. Adhikari, S.C. Das, R. Roy, S. Pramanick, K. De, O. Ivashko, A. C. Dippel, M. von Zimmermann, S. Bandyopadhyay, R. Mondal, S. Chatterjee, Impact of incomplete martensitic phase transition on the magnetic behavior of Co-doped MnNiGe1.05 alloys, Phys. Rev. B 109 (2024) 144420.
[40] W.H. Guo, X.F. Miao, Z.B. Yan, Y.L. Chen, Y. Gong, F.J. Qian, F. Xu, L. Caron, Colossal negative thermal expansion over a wide temperature span in dynamically self-assembled MnCo(Ge,Si)/epoxy composites, Mater. Res. Lett. 12 (2024) 315.
[41] L. Caron, Z.Q. Ou, T.T. Nguyen, D.T.C. Thanh, O. Tegus, E. Brück, On the determination of the magnetic entropy change in materials with first-order transitions, J. Magn. Magn. Mater. 321 (2009) 3559.
[42] H.M. Rietveld, A profile refinement method for nuclear and magnetic structures, J. Appl. Crystallogr. 2 (1969) 65.
[43] J. Cízek, Characterization of lattice defects in metallic materials by positron annihilation spectroscopy: a review, J. Mater. Sci. Technol. 34 (2018) 577.
[44] R.B. Strozi, M. Witman, V. Stavila, J. Cizek, K. Sakaki, H. Kim, O. Melikhova, L. Perrière, A. Machida, Y. Nakahira, G. Zepon, W.J. Botta, C. Zlotea, Elucidating primary degradation mechanisms in high-cycling-capacity, compositionally tunable high-entropy hydrides, Acs. Appl. Mater. Inter. 15 (2023) 38412.
[45] F. Becvár, J. Cízek, I. Procházka, J. Janotová, The asset of ultra-fast digitizers for positron-lifetime spectroscopy, Nucl. Instrum. Meth. A 539 (2005) 372.
[46] J. Cízek, PLRF code for decomposition of positron lifetime spectra, Acta Phys. Pol. a 137 (2020) 177.
[47] J. Cízek, M. Vlcek, I. Procházka, Digital spectrometer for coincidence measurement of doppler broadening of positron annihilation radiation, Nucl. Instrum. Meth. A 623 (2010) 982.
[48] G. Kresse, J. Furthmuller, Efficient iterative schemes for ab initio total-energy calculations using a plane-wave basis set, Phys. Rev. B 54 (1996) 11169.
[49] F. Guillou, V. Hardy, Burst-like features observed from different techniques at the first-order magnetic transition of La(Fe,Co,Si)13, J. Alloy. Compd. 977 (2024) 173161.
[50] S. Smiy, A. Omri, R. Moussi, A. Ben Ali, S. Hcini, B.F.O. Costa, E.K. Hlil, E. Dhahri, Influence of non-magnetic Ti4+ ion doping at Mn site on structural, magnetic, and magnetocaloric properties of La0.5Pr0.2Sr0.3Mn1xTixO3 manganites (x=0.0 and 0.1), J. Supercond. Nov. Magn. 32 (2019) 1653.
[51] T. Krenke, M. Acet, E.F. Wassermann, X. Moya, L. Mañosa, A. Planes, Ferromagnetism in the austenitic and martensitic states of Ni-Mn-In alloys, Phys. Rev. B 73 (2006) 174413.
[52] E.K. Liu, W.H. Wang, L. Feng, W. Zhu, G.J. Li, J.L. Chen, H.W. Zhang, G.H. Wu, C. B. Jiang, H.B. Xu, F.R. de Boer, Stable magnetostructural coupling with tunable magnetoresponsive effects in hexagonal ferromagnets, Nat. Commun. 3 (2012) 873.
[53] Y.J. Zhang, Q.Q. Zeng, Z.Y. Wei, Z.P. Hou, Z.H. Liu, E.K. Liu, X.K. Xi, W.H. Wang, X.Q. Ma, G.H. Wu, Cluster spin glass state caused by antiphase boundaries in NiFeGa alloys, J. Alloy. Compd. 749 (2018) 134.
[54] G. Yu, H.X. Chen, S.C. Ma, X.H. Luo, C.F. Liu, C.C. Chen, C.S. Fang, Y.W. Yuan, X. Y. Ye, Z.C. Zhong, Robust topological Hall effect in a reentrant spin glass system Mn1.89Pt0.98Ga1.12, Physica B 640 (2022) 414043.
[55] Y.F. Tang, Y. Umemoto, Y. Kawamoto, M. Kawamata, S. Asai, Y. Ikeda, M. Fujita, Y. Nambu, Unusual spin dynamics in the van der Waals antiferromagnet FeGa2S4, J Phys.-Condens Mat. 37 (2025) 035801.
[56] V.G.D. Paula, V.M. Andrade, M. Reis, Multifunctional compounds: a comparative review towards all-d hexagonal ferromagnets, J. Alloy. Compd. 963 (2023) 171009.
[57] F.Q. Zhang, P.J. Feng, A. Kiecana, Z.Y. Wu, Z.W. Bai, W.J. Li, H.C. Chen, W. Yin, X. W. Yan, F.J. Ma, N.V. Dijk, E. Brueck, Y. Ren, Achieving tunable high-performance giant magnetocaloric effect in hexagonal Mn-Fe-P-Si materials through different d-block doping, Adv. Funct. Mater. (2024) 2409270.
[58] O. Gutfleisch, T. Gottschall, M. Fries, D. Benke, I. Radulov, K.P. Skokov, H. Wende, M. Gruner, M. Acet, P. Entel, M. Farle, Mastering hysteresis in magnetocaloric materials, Philos. T R Soc. A 374 (2016) 20150308.
[59] L.F. Cohen, Contributions to hysteresis in magnetocaloric materials, Phys. Status. Solidi. B 255 (2018) 1700317.
[60] X.F. Miao, Y. Gong, F.Q. Zhang, Y.R. You, L. Caron, F.J. Qian, W.H. Guo, Y. J. Zhang, Y.Y. Gong, F. Xu, N. van Dijk, E. Brück, Enhanced reversibility of the magnetoelastic transition in (Mn,Fe)2(P,Si) alloys via minimizing the transition-induced elastic strain energy, J. Mater. Sci. Technol. 103 (2022) 165.
[61] K.A. Gschneidner, Y. Mudryk, V.K. Pecharsky, On the nature of the magnetocaloric effect of the first-order magnetostructural transition, Scripta. Mater. 67 (2012) 572.
[62] J. Liu, Y.R. You, I. Batashev, Y.Y. Gong, X.M. You, B.W. Huang, F.Q. Zhang, X. F. Miao, F. Xu, N. van Dijk, E. Brück, Design of reversible low-field magnetocaloric effect at room temperature in hexagonal MnMX ferromagnets, Phys. Rev. Appl. 13 (2020) 054003.
[63] W. Bazela, A. Szytuła, J. Todorović, Z. Tomkowicz, A. Zięba, Crystal and magnetic structure of NiMnGe, Phys. Status Solidi (a) 38 (1976) 721.
[64] W. Hanggai, O. Tegus, H. Yibole, F. Guillou, Structural and magnetic phase diagrams of MnFe0.6Ni0.4(Si,Ge) alloys and their giant magnetocaloric effect probed by heat capacity measurements, J. Magn. Magn. Mater. 494 (2020) 165785.
[65] M.F.J. Boeije, P. Roy, F. Guillou, H. Yibole, X.F. Miao, L. Caron, D. Banerjee, N. H. van Dijk, R.A. de Groot, E. Brück, Efficient room-temperature cooling with magnets, Chem. Mater. 28 (2016) 4901.
[66] X.F. Miao, Y. Gong, L. Caron, Y.R. You, G.Z. Xu, D. Sheptyakov, P. Manuel, F. J. Qian, Y.J. Zhang, F. Xu, N. van Dijk, E. Brück, Switching the magnetostructural coupling in MnCoGe-based magnetocaloric materials, Phys. Rev. Mater. 4 (2020) 104407.
[67] F.R. Shen, H.B. Zhou, F.X. Hu, J.T. Wang, H. Wu, Q.Z. Huang, J.Z. Hao, Z.B. Yu, Y. H. Gao, Y. Lin, Y.X. Wang, C. Zhang, Z. Yin, J. Wang, S.H. Deng, J. Chen, L.H. He, T.J. Liang, J.R. Sun, T.Y. Zhao, B.G. Shen, A distinct spin structure and giant baromagnetic effect in MnNiGe compounds with Fe-doping, J. Am. Chem. Soc. 143 (2021) 6798.
[68] F.Q. Zhang, I. Batashev, N. van Dijk, E. Brück, Reduced hysteresis and enhanced giant magnetocaloric effect in B-doped all-d-metal Ni-Co-Mn-Ti-based Heusler materials, Phys. Rev. Appl. 17 (2022) 054032.
[69] F.Q. Zhang, I. Batashev, Q. Shen, Z.Y. Wu, R.I. Smith, G.A. de Wijs, N. van Dijk, E. Brück, Impact of F and S doping on (Mn,Fe)2(P,Si) giant magnetocaloric materials, Acta Mater. 234 (2022) 118057.
[70] W.H. Guo, X.F. Miao, J.Y. Cui, S. Torii, F.J. Qian, Y.Q. Bai, Z.D. Kou, J.J. Zha, Y. Y. Shao, Y.J. Zhang, F. Xu, L. Caron, Significantly enhanced reversibility and mechanical stability in grain-oriented MnNiGe-based smart materials, Acta Mater. 263 (2024) 119530.
[71] Z. Gercsi, K.G. Sandeman, Structurally driven metamagnetism in MnP and related pnma compounds, Phys. Rev. B 81 (2010) 224426.
[72] A. Barcza, Z. Gercsi, K.S. Knight, K.G. Sandeman, Giant magnetoelastic coupling in a metallic helical metamagnet, Phys. Rev. Lett. 104 (2010) 247202.
[73] C. Yang, J.P. Wharry, Role of point defects in stress-induced martensite transformations in NiTi shape memory alloys: a molecular dynamics study, Phys. Rev. B 105 (2022) 144108.
[74] K. Sohlberg, T.J. Pennycook, W. Zhou, S.J. Pennycook, Insights into the physical chemistry of materials from advances in HAADF-STEM, Phys. Chem. Chem. Phys. 17 (2015) 3982.
[75] D.R. Liu, D.Y. Wang, T. Hong, Z.Y. Wang, Y.P. Wang, Y.X. Qin, L.Z. Su, T.Y. Yang, X. Gao, Z.H. Ge, B.C. Qin, L.D. Zhao, Lattice plainification advances highly effective SnSe crystalline thermoelectrics, Science (1979) 380 (2023) 841.
[76] H.M. Pang, Y.T. Qiu, D.Y. Wang, Y.X. Qin, R. Huang, Z.Z. Yang, X. Zhang, L. D. Zhao, Realizing N-type SnTe thermoelectrics with competitive performance through suppressing Sn vacancies, J. Am. Chem. Soc. 143 (2021) 8538.
[77] F.A. Selim, Positron annihilation spectroscopy of defects in nuclear and irradiated materials- a review, Mater. Charact. 174 (2021) 110952.
[78] F. Tuomisto, Identification of point defects in multielement compounds and alloys with positron annihilation spectroscopy: challenges and opportunities, Phys. Status Solidi-R 15 (2021) 2100177.
[79] F.Q. Zhang, Z.Y. Wu, J.L. Wang, W.Y. Chen, Z.D. Wu, X. Chi, C.L. Zhao, S. Eijt, H. Schut, X.D. Bai, Y. Ren, N. van Dijk, E. Brück, Impact of fast-solidification on all-d-metal NiCoMnTi based giant magnetocaloric heusler compounds, Acta Mater. 265 (2024) 119595.
[80] R.W. Siegel, Positron annihilation spectroscopy, Annual. Rev. Mater. Sci. 10 (1980) 393.
[81] F. Tuomisto, I. Makkonen, Defect identification in semiconductors with positron annihilation: experiment and theory, Rev. Mod. Phys. 85 (2013) 1583.
[82] J.M.C. Robles, E. Ogando, F. Plazaola, Positron lifetime calculation for the elements of the periodic table, J. Phys.-Condens Mat. 19 (2007) 176222.
[83] Q.G. Yang, X.Z. Cao, B.Y. Wang, P. Wang, Systematic investigation of positron annihilation in transition metals from first principles, Phys. Rev. B 108 (2023) 104113.
[84] J. Cízek, T. Vlasák, O. Melikhova, Characterization of lattice defects in refractory metal high-entropy alloy HfNbTaTiZr by means of positron annihilation spectroscopy, Phys. Status. Solidi A 219 (2022) 2100840.
[85] D.E. Jodi, T.A. Listyawan, P. Hruska, J. Cizek, N. Park, U. Lee, Study of vacancies in Fex(CoCrMnNi)100-x medium- and high-entropy alloys by positron annihilation spectroscopy, Scripta Mater. 194 (2021) 113654.